Rheological behavior of gel polymer electrolytes: yield stress and viscoelasticity

Diego Milián, Denis C D Roux, François Caton, Nadia El Kissi

Gel polymer electrolytes rheological behavior: yield stress and viscoelasticity

Journal:	*Rheologica Acta*
Manuscript ID	Draft
Manuscript Type:	Original Contribution
Keywords:	Yield stress, Gel, Herschel-Bulkley, Liquid-solid transition, Couette analogy, Redox flow batteries
Note: The following files were submitted by the author for peer review, but cannot be converted to PDF. You must view these files (e.g. movies) online.	
instability10_1.mp4	

Gel polymer electrolytes rheological behavior: yield stress and viscoelasticity

Diego Milián[a], Denis C.D. Roux[a], François Caton[a], Nadia El Kissi[a]

[a]*Univ. Grenoble Alpes, CNRS, Grenoble INP, LRP, 38000 Grenoble, France*

Corresponding author: Nadia El Kissi e-mail: nadia.elkissi@univ-grenoble-alpes.fr

ORCID (Diego Milián): 0000-0002-1798-2384

Keywords: Yield stress, Gel, Herschel-Bulkley, Liquid-solid transition, Couette analogy, Redox flow batteries

Abstract

In redox flow batteries (RFBs), semi solid flow cells incorporate solid particles in the same medium than the electrolyte in the form of slurry to increase energy efficiency. However, rheological properties of the fluid hosting the solid particles need to favor particle stability and pumping process within the RFB. In this study, the materials used to formulate a gelled polymer electrolyte (GPE), that will be used as suspending fluid for dense zinc microparticles in a zinc slurry - air RFB, were studied. It was found that when using polyacrylic acid and attapulgite gelling agents together, a yield stress behavior was obtained. This satisfactory result was accomplished even in harsh alkaline conditions (pH > 14), representative of the battery operation conditions in which the chemical stability of gelling agents is threatened. Yield stress values were obtained by fitting experimental data to the Herschel-Bulkley model and results were compared to creeps. Results indicate that the GPEs presented in this study are good candidates to host zinc microparticles for a zinc slurry - air RFB.

Introduction

Since late 20th century, Li-ion batteries have dominated the energy storage market (Li et al. 2018), but market-dependent cost (Ciez and Whitacre 2016), limited geological availability (Gruber et al. 2011; Vikström et al. 2013), fire-related hazards (Kong et al. 2018) and recyclability (Garole et al. 2020) have taken academia and industry to search for more sustainable solutions for the future. Recently, redox flow batteries (RFBs) have gained attention because of its flexible design, outstanding from others electrochemical energy storage systems.

Redox flow batteries (RFBs) are energy storage systems that aim to shorten the gap between intermittent renewable energy sources like wind and solar, and the energy grid (Rugolo and Aziz 2012). RFBs differ from regular batteries because electrolytes are stored externally in reservoirs and pumped throughout the reactor, where power generation and energy storage take place. RFB storage capacity will depend on the size of the electrolyte tanks, whereas power output will depend on the number of cells within the battery stack. In the electrolyte tanks, energy is stored in electro-active materials dissolved or dispersed in aqueous electrolytes. The ability of redox-active materials to be oxidized and

reduced indefinitely gives the battery the capability of being rechargeable. This flexible design allows independent storage/power optimization and easy scalability for specific applications.
Recently, metal-air batteries have been designed as RFBs. Advantageous high energy density, inherent of metals (Kim et al. 2013; Han et al. 2018), combined with the flexible design of RFBs, able to decouple energy and power, have been investigated under this synergistic approach. Amongst them, zinc – air RFB have gained special attention due to zinc availability on earth and its high specific energy density (1350 Wh/kg (Bockelmann et al. 2016)).

Nonetheless, metallic zinc anode suffers from different stability problems during charging such as localized dendrite formation (Banik and Akolkar 2015; Liu et al. 2016; Yang et al. 2016), electrode shape change (Mainar et al. 2018a) and formation of passivation layers (Yang et al. 2004; Han et al. 2018). Consequently, new approaches are being evaluated to enhance battery lifespan, among them, the development of a semi-solid zinc anode consisting in zinc microparticles dispersed in alkaline electrolyte forming a slurry.

When using a slurry approach, zinc works as a flowable anode (semi-solid electrode) which is stored in a tank externally to the reactor. Thus, zinc slurry serves the double purpose of electrode and electrolyte, reaching higher energy densities due to utilization of active material in comparison with its equivalent pure aqueous electrolyte configuration (Duduta et al. 2011). When battery is under operation, slurry is pumped to the reactor where charge/discharge reactions take place. Moreover, slurry viscosity needs to be sufficiently low to be able to be pumped throughout the battery without affecting the energetic efficiency of the RFB (Iyer et al. 2017; Barton et al. 2018).

Zinc slurry flow behavior is of great importance to the whole system, not only when the battery is operating but also at rest. The properties that are sought in the suspending fluid consist in a dual behavior explained as follows. First, the viscosity has to be high enough to maintain dense microparticles in suspension (ρ_{zinc} = 7.13 g/cm^3) when the battery is at rest. Secondly, the viscosity should decrease during the battery operation, allowing to ease the pumping towards the cell stack within the RFB. Finally, this dual viscous behavior ought to be stable in harsh alkaline environment (pH > 14), conditions at which gelling agents able to suspend dense zinc particles are scarce. Alkaline conditions are chosen because of the high ionic conductivity favoring the transport of specific zinc ionic species and zinc stability in aqueous media (Mainar et al. 2018b, c). Hence, an optimal formulation for the suspending fluid has to be found in order to comply with the above statements.

In this study, the rheology of the suspending fluids for anode zinc slurries is thoroughly analyzed. Gelled polymer electrolytes (GPEs) are proposed as suspending fluids for zinc particles to be used in a zinc slurry - air RFB. GPEs considered consist in a gelled potassium hydroxide (KOH) electrolyte. KOH has been used previously in zinc slurry - air application (Mainar et al. 2016, 2018b; Gu et al. 2017), because of its superior conductivity to other alkaline electrolytes. In order to form a gelled electrolyte two different gelling agents are used: polyacrylic acid (PAA) and attapulgite.

PAA forms a physical gel with enhanced viscosity at neutral pH (Piau 2007). Although previous studies have shown that viscosity of PAA decreases significantly at pH higher than 10 (Lochhead et al. 1989; Charman et al. 1991; Gutowski et al. 2012), it has been shown that PAA is able to remain chemically stable under highly alkaline KOH concentrations (Tran et al. 2019)for zinc-air battery application.

To further strengthen network gel properties, attapulgite clay is used in the formulation. Attapulgite is a magnesium aluminium silicate clay with chemical formula $3MgO\text{-}1.5Al_2O_3\text{-}8SiO_2\text{-}9H_2O$. This clay forms a gel when mixing at high shear rates, breaking aggregates dispersing evenly the particles. Attapulgite has been previously used to formulate zinc anode slurries. In addition, it was found that when used as additive together with zinc oxide (ZnO) in the formulation, battery life is improved as less corrosion rates are reported (Sonneveld 1991).

Ideally a slurry RFB should behave as a yield stress fluid. Indeed, yield stress fluids are materials that displays a dual flow behavior: at stresses below yield stress (τ_y), materials will show solid-elastic behavior and at stresses above yield stress, material will start to flow and behave as a viscous liquid following a shear-thinning behavior. Different models have been proposed to analyze yield stress fluids. The Herschel-Bulkley model usually describes properly the rheology of suspensions using 3 parameters (Ovarlez et al. 2015; Frigaard 2019). This model is expressed in equation 1:

$$\tau = \tau_y + K\dot{\gamma}^n \qquad (1)$$

Where τ is the shear stress, $\dot{\gamma}$ is the shear rate and the 3 parameters correspond to: τ_y yield stress, *K* consistency index, and *n* flow index.

This study aims to characterize elasto-visco-plastic behavior of GPEs containing high concentration of electrolytes designed for energy storage. Yield stress flow behavior is sought for RFB application at pH > 14, conditions in which gelling agents as PAA behave poorly as suspending fluids. Notably, the effect of PAA concentration in GPEs is studied to evaluate gelled network properties as candidates to be used in a RFB. Samples are studied using small and large deformation rheological tests. Oscillatory rheology is used to study viscoelastic sample properties in the linear regime representative of the material at rest. Steady state flow curves are obtained for each of the samples analyzed using large deformation techniques from which yield stresses were determined using Herschel-Bulkley model (equation 1). Moreover, GPEs yielding was studied performing creep tests, allowing to study and compare liquid-solid transition. With the objective to determine if sample exhibited time-dependent properties (i.e. thixotropy, structuration) (Møller et al. 2006; Caton and Baravian 2008; Dinkgreve et al. 2016), GPEs viscoelastic properties were linked and analyzed using rheometer rotor inertia (Baravian and Quemada 1998; Auffret et al. 2009; Benmouffok-Benbelkacem et al. 2010) during creeps. This set of tests provided detailed rheological properties of solid and liquid regimes of GPEs.

Materials and methods

Sample preparation

GPEs are prepared as follows. Aqueous electrolyte solution was prepared by dissolving potassium hydroxide (KOH) flakes (Reagent grade, 90 %, Sigma-Aldrich) in deionized water. The resulting pH of this solution was found to be 14.7 obtained with a pH meter (Orion Star A215, Thermo Fisher Scientific), using a pH/ATC rechargeable electrode (Orion™ ROSS Ultra™ Triode™). Next PAA gelling agent (Carbopol® 940, Acros Organics) was dissolved in aqueous electrolyte solution with the aid of a magnetic stirrer for 24 h to ensure full polymer dissolution. Then, attapulgite gelling agent (Attagel® 50, BASF), was added to the mixture together with zinc oxide (99.9 % metal basis, -200 mesh powder, Alfa Aesar), under continuous stirring for 5 minutes. Finally, mixture was homogenized during 1 minute using a high shear homogenizer (Ultra-Turrax, T25 model, IKA) to obtain the GPE. Samples were mixed at the lowest speed (11 000 rpm for 1 minute) to avoid mechanical degradation of PAA chains and to disperse and build attapulgite gel.

Concentrations of each component are available in table 1. It is remarked that this study is focused on the effect of PAA gelling agent on GPEs rheological behavior. Concentrations were carefully chosen and tested in the set-up presented in one of our studies on a zinc slurry-air RFB (Choi et al. 2020a). Alkaline environment for the operation of the battery together with ionic conductivity were obtained from KOH electrolyte at a concentration of 92 % wt. PAA and attapulgite concentrations were chosen to prepare gel materials. Finally, ZnO was added to prevent zinc self-discharge. As shown by N. Choi et al. (Choi et al. 2020a, b), satisfactory discharge results were obtained using a similar formulation with same electrolyte KOH concentration.

Sample	KOH 10 M [wt. %]	PAA [wt. %]	Attapulgite [wt. %]	ZnO [wt. %]
GPE1	92.00*	0.30	1.40	6.00
GPE2		0.45		
GPE3		0.60		
GPE4		0.75		
GPE5		0.90		

Table 1. Gel polymer electrolytes (GPEs) composition.
*Depending on the concentration of PAA, the concentration of KOH 10 M is modified so the sum of all components equals 100%.

Rheometry

GPEs rheological behavior was investigated using a stress-controlled rheometer AR-G2 (TA instruments, United States) equipped with a specially designed 4-blade vane-in-cup geometry (h = 45.5 mm, d = 30 mm), as depicted in figure 1. Vane-in-cup tool was used to avoid slippage (Barnes and Nguyen 2001), and ensure sample homogeneity (Aït-kadi et al. 2002). A transparent cup (D = 48 mm) was used to observe the appearance of sheared sample with the aid of microscope USB camera (A1 2MP 500 X, Andonstar, China). The wall of the cup was equipped with a squared grid (L_{square} = 5.5 mm, *thickness* = 2 mm) to suppress slippage between the sample and cup wall (Owens et al. 2020).

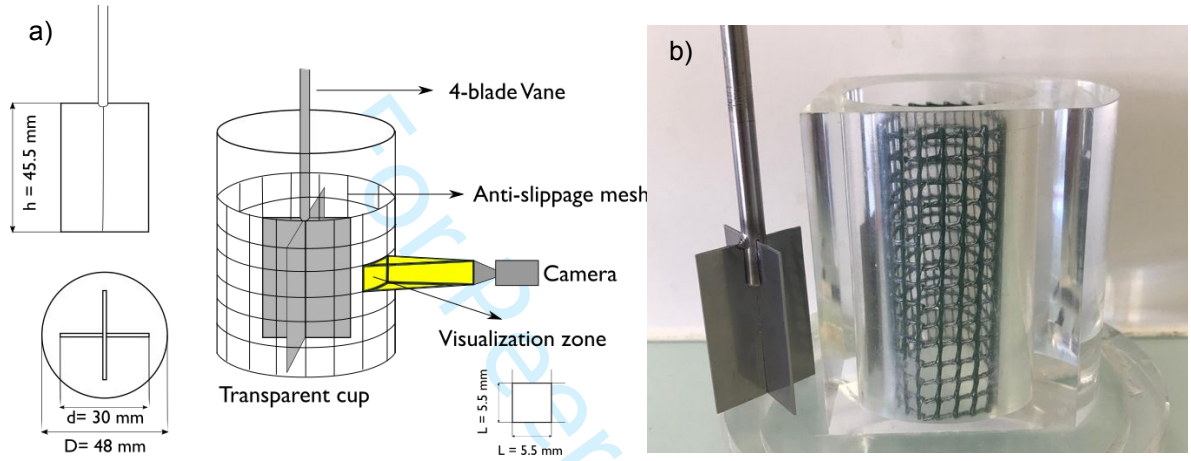

Figure 1. Vane-in-cup shearing geometry. Transparent cup allows to observe sample appearance trough the spaces of the squared grid (L_{square} = 5.5 mm and *thickness* 2 mm). a) Scheme of Vane-in-cup and set up used for GPEs rheometric characterization. b) Picture of actual set-up.

The vane generates a flow profile similar to the one occurring in concentric cylinders geometry (Baravian et al. 2002; Ovarlez et al. 2011). Furthermore, it is possible to convert rotational speed and torque obtained with the vane-in-cup, into shear rate and shear stress, respectively, using a Couette analogy approach (Aït-kadi et al. 2002). Figure 2 is a representation of the Couette analogy applied for the vane-in-cup used in this study.

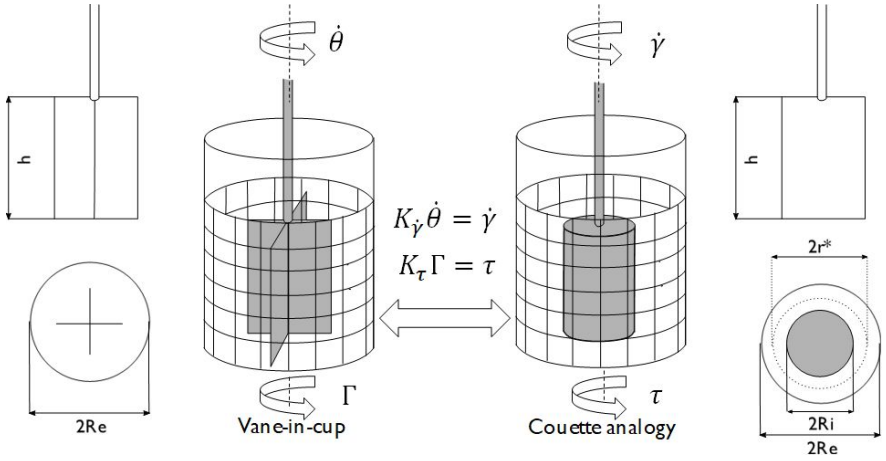

Figure 2. Vane geometry and its virtual analogous cylinder, modified from (Aït-kadi et al. 2002).

In the scheme in figure 2, $K_{\dot{\gamma}}$ and K_{τ} are geometrical factors that need to be experimentally determined. Once factors are obtained, they can be applied as if the geometry used is an analogous inner cylinder and so shear rate and shear stress can be calculated as follows (Aït-kadi et al. 2002; Hermoso et al. 2012; Puig et al. 2016):

$$\dot{\gamma} = K_{\dot{\gamma}}\dot{\theta} \qquad (2)$$

$$\tau = K_{\tau}\Gamma \qquad (3)$$

Where $\dot{\theta}$ is the rotational velocity, Γ is the measured torque and $K_{\dot{\gamma}}$ and K_{τ} are the geometrical correction factors.

Geometrical factors were determined using the Couette analogy introduced by Aït-Kadi et al. (Aït-kadi et al. 2002). This protocol determines analogous inner cylinder dimensions, represented in figure 2, corresponding to the flow profile generated by the Vane. $K_{\dot{\gamma}}$ and K_{τ} were determined as follows:

$$K_{\dot{\gamma}} = \frac{\frac{2}{n}\left(\frac{R_e}{r^*}\right)^{\frac{2}{n}}}{\left(\frac{R_e}{R_i}\right)^{\frac{2}{n}} - 1} \qquad (4)$$

$$K_{\tau} = \frac{1}{2\pi r^{*2} h} \qquad (5)$$

Where R_e and R_i are the cup and the analogous inner cylinder radius, respectively, *h* is the height of the vane, corresponding to the height of the analogous inner cylinder; *n* is the flow index of the fluid used for the calibration and *r** is an optimal radial position calculated from cup and vane dimensions. At this position *r**, any sample can be characterized independently of its flow index *n*.

A shearing experiment with a standard Newtonian fluid (ISO 17025, 6166 mPa s, 20 °C, Paragon Scientific Ltd), was done to perform the calibration. This fluid was selected to perform the calibration because its viscosity corresponds to the same order of magnitude than the samples analyzed in this study in its fluidized state (above yield stress).

Complete calculation of analogous inner cylinder radius R_i and optimal radial position r* can be found in the paper by Aït-Kadi et al. (Aït-kadi et al. 2002) and in supplementary information S1. With these conditions, $K_{\dot{\gamma}}$ = 2.30 rad^{-1} and K_{τ} = 13450.7 Pa N^{-1}m^{-1} were obtained. Calibration was successfully validated by measuring the viscosity of a non-Newtonian fluid (Carbopol® 940 0.10 wt. %). Results obtained with the vane tool were compared to the ones obtained with a cone (1 deg, *r* = 30 mm) and plate geometry (see supplementary information S1).

GPEs Oscillatory rheometry

GPEs viscoelastic properties at small deformations are studied by oscillatory rheometry by applying sinusoidal deformations. Linear domain was obtained by performing a strain amplitude sweep tests, from 0.1 to 1000 % at 1 Hz.

After determining linear domain, samples viscoelastic behavior at rest was studied. This was done by performing a frequency sweep from 0.01 to 4 Hz at a constant deformation γ = 0.1%, located in sample linear domain.

GPEs flow curves

GPEs flow curves were obtained by large deformation tests. For such complex materials a specific protocol had to be implemented in order to obtain results representative of the material and independent of sample previous handling or shear history before its characterization. To do so, the protocol was first tested and optimized with GPE5 sample. Successive shear rate steps are applied from 0.001 to 100 s^{-1} and down to 0.001 s^{-1}, each step with a duration of 120 s (5 measured points per decade). This shear rate increase and decrease was repeated twice, as represented in figure 3a. This was done in order to understand if the solid-liquid transition is comparable to the liquid-solid transition, and the reproducibility of the measurement when comparing the ramps.

Shear stress response to applied shear rate is represented in figure 3b. During the first increasing steps (curve Up 1), it is observed that shear stress increases continuously in a shear-thinning behavior. As the first decreasing steps starts (Down 1), shear stress recorded is lower than the value obtained for the first increasing ramp. As shear rate decreases to the lowest values, a clear shear stress plateau is observed, indicating yield stress behavior. The subsequent Up 2 and Down 2 ramps are superimposed

to the first Down 1, showing excellent reproducibility once the material mechanical history has been erased by the first increasing ramp.

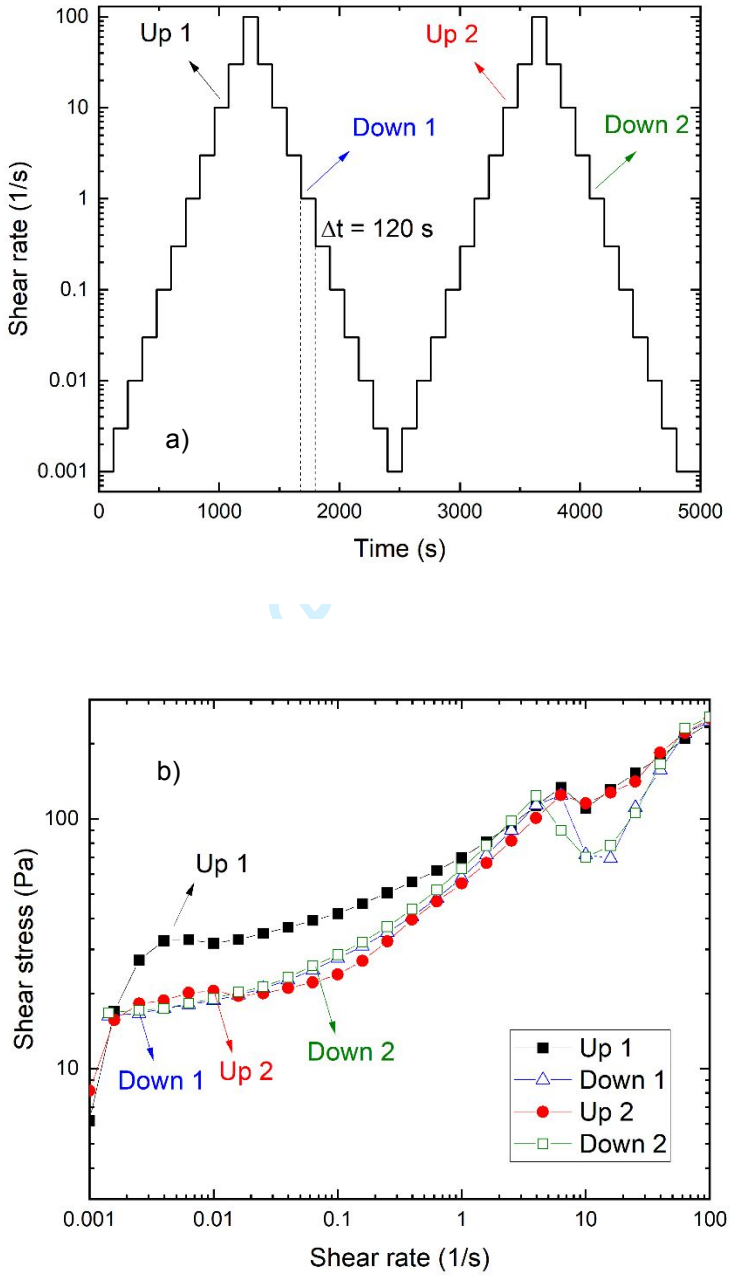

Figure 3. a) Flow sweep protocol. Sample undergoes consecutively increasing and decreasing shear rate steps from 0.001 to 100 s^{-1} and down to 0.001 s^{-1}. Each step had a duration of 120 s, 5 points per decade were obtained with a total of 25 steps. b) GPE5 shear stress as function of shear rate. Numbers correspond to the order in which flow sweeps were performed.

However, at shear rates higher than 3 s^{-1}, stress suddenly undershoots independently of the ramp. This sudden decrease in shear stress is a consequence of the Weissenberg effect (Weissenberg 1947;

Eitelberg 1984) and more information can be found in supplementary information S2, together with a video. At shear rates lower than 3 s^{-1}, Weissenberg effect is not observed and results are reproducible in this region. The flow behavior is the one of a yield stress fluid followed by shear thinning behavior. Furthermore, pictures of the sample in the transparent cup were taken during shearing through the spaces of the grid (figure 1a), and they can be observed in the insets in the figure in supplementary information S3. It is observed that when shear rate is up-ramped for the first time (Up 1), sample appearance changes from a plain surface aspect (at $\dot{\gamma}$ = 0.01 s^{-1}) to small aggregates across all the sample at $\dot{\gamma} \geq 0.01$ s^{-1}. Contrarily, when shear rate is down-ramped (Down 1), changes in sample appearance are not observed. In fact, when aggregates are seen across all the sample, the appearance of the sample will not further change. To summarize information above, when sample undergo the first solid-liquid transition (Up 1), the appearance of the sample changes and adopt a new flow behavior, with a lower yield stress. Once the sample adopt the new appearance, flow behavior remains the same (curves Down 1 and Down 2), as sample aspect does not further evolve. A small deviation is observed for curve Up 2, indicating that indeed decreasing ramps must be used for this sample to obtain reproducible results at shear rates ≤ 3 s^{-1}.

Thus, steady state flow curves for all samples GPE1 - GPE5 were obtained only by down-ramping shear rate steps, unless stated for a specific result. Each decreasing step had a duration of Δt = 1000 s, sufficient to attain steady state as shown in figure supplementary information S2, unless otherwise indicated.

To quantify rheological parameters of GPEs, shear stress as function of shear rate experimental data is fitted to a Herschel-Bulkley model (equation 1), from which yield stress τ_y, consistency index *K* and flow index *n* are obtained, describing sample flow behavior.

Creeps

Samples elasto-visco-plastic behavior was studied using creep tests. Focus was placed on solid-liquid and liquid-solid transition to determine sample yield stress. Moreover, this yielding study allowed comparison to yield stress obtained from fitting experimental flow curves data to Herschel-Bulkley model (equation 1).

Several studies (Cheng 1986; Ovarlez et al. 2013; N'gouamba et al. 2020), have found two type of yield stresses being the **static** yield stress and the **dynamic** yield stress. Tests to determine yield stress assess whether the sample in evaluation has developed a steady state flow (**static** yield stress) or has ceased flowing (**dynamic** yield stress). Experimental efforts have shown that static yield stress is higher than dynamic yield stress, for the same material analyzed (Cheng 1986). Therefore, the protocol presented in this section will allows us to determine how different is the yield stress depending on the direction in which the solid-liquid transition is studied (Benmouffok-Benbelkacem et al. 2010).

To set up the creep protocol, preliminary τ_y values were used as reference for each GPE in the following way. Shear stresses were increased from $\tau_{initial}$ (below yield stress) to τ_{final} (above yield stress), and then decreasing back to $\tau_{initial}$, as shown in figure 4a. Equivalently, values of $\tau_{initial}$ and τ_{final} were carefully selected from flow curves for each GPE, so the solid-liquid transition could be observed. Finally, to ensure steady state each creep step had a duration of Δt = 1000 s. Figure 4b shows the expected strain response as function of time of the viscoelastic material when a stress is applied to it.

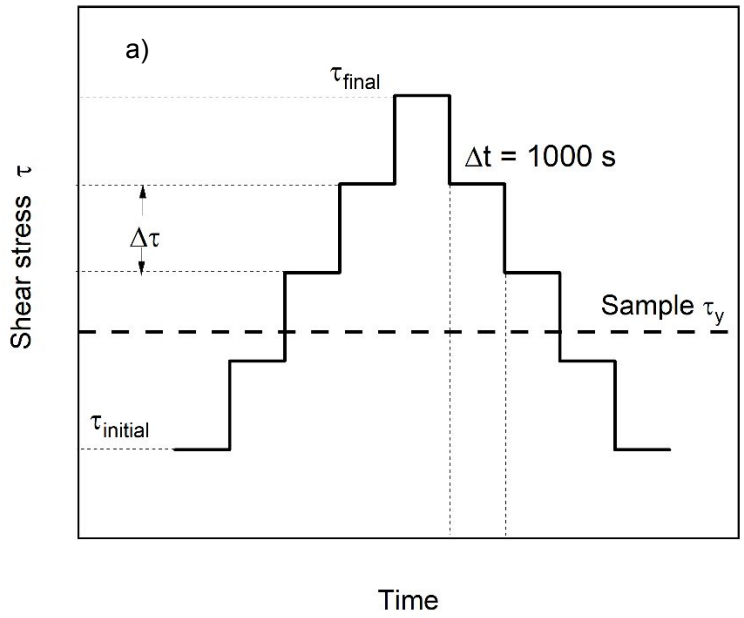

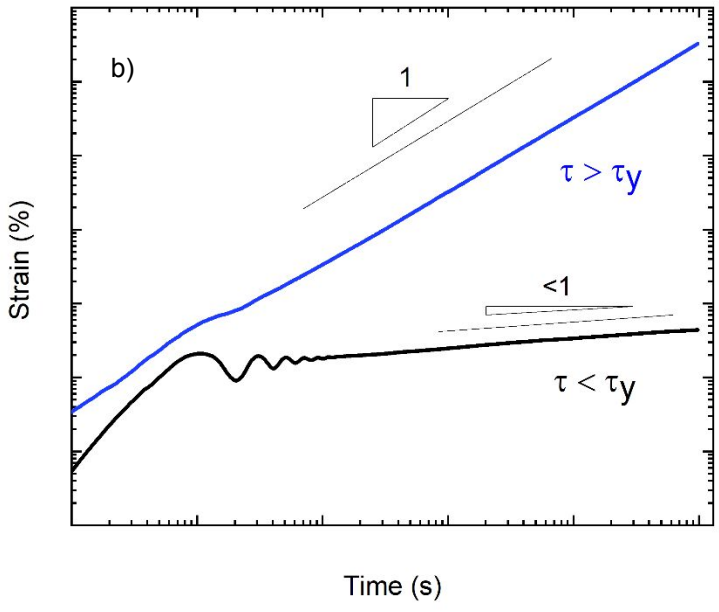

Figure 4. Creep protocol for GPEs. a) Successive creeps procedure to determine yielding. Each creep step had a duration of 1000 s. b) Example of expected response to creep procedure.

It is observed in figure 4b that two behaviors can be expected depending if the stress τ is smaller or larger than sample τ_y. When $\tau < \tau_y$, strain evolves as a weak power law over time, characteristic of solid-like state. Contrarily, when $\tau > \tau_y$, strain increases rapidly as function of time with a slope of 1, indicating that the sample is flowing in steady state.

Furthermore, figure 4b also shows strain oscillations during creep experiments. These oscillations have an elastic origin and are helpful to study the influence of time and shear history on viscoelastic properties of GPEs. This is explained in detail in next section.

Inertio-elastic oscillations

In this section, a method is presented in which sample viscoelastic properties are obtained from creep oscillations. As observed in figure 5, when performing creep experiments, deformation oscillates at the beginning of each creep step. This response is known as inertio-elastic oscillations (Baravian and Quemada 1998; Yao et al. 2008).

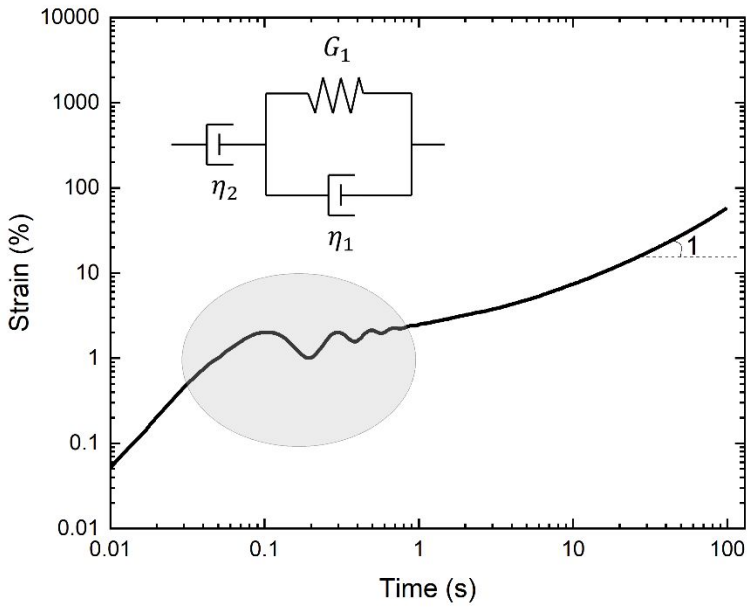

Figure 5. Creep test highlighting inertio-elastic oscillations. Inset is a representation of the Jeffrey model representing sample viscoelastic properties.

In figure 5, oscillations are seen as a result of the inertial response of the moving part of the rheometer and the viscoelastic sample. A Jeffrey model (inset figure 5) is proposed to analyze these oscillations and link them to sample viscoelasticity. The model consists in a dashpot element in series with another element composed by a dashpot connected in parallel to a spring. The dash-pot represents viscous

liquid behavior of the sample η_2, whereas the elements in parallel represents the elasticity *G* and elastic dissipation η_1.

The constitutive equation of Jeffrey model is (Baravian and Quemada 1998):

$$(\eta_1 + \eta_2)\dot{\tau} + G\tau = \eta_2 G\dot{\gamma} + \eta_1\eta_2\ddot{\gamma} \qquad (6)$$

The analytical solution of this equation if found in the paper of Benmouffok-Benbelkacem et al. (Benmouffok-Benbelkacem et al. 2010), in which strain γ is described by a function involving the inertia of the rotating geometry and the viscoelastic sample information that will be obtained by the model being η_1, η_2, and *G*.

Results

Oscillatory rheometry

Viscoelastic GPEs properties were studied by means of oscillatory rheometry and results are depicted in figure 6.

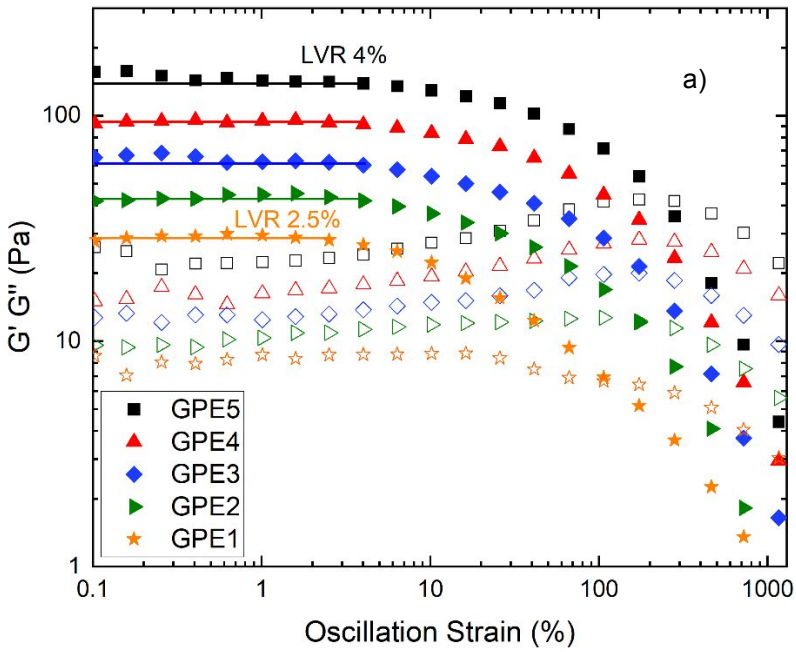

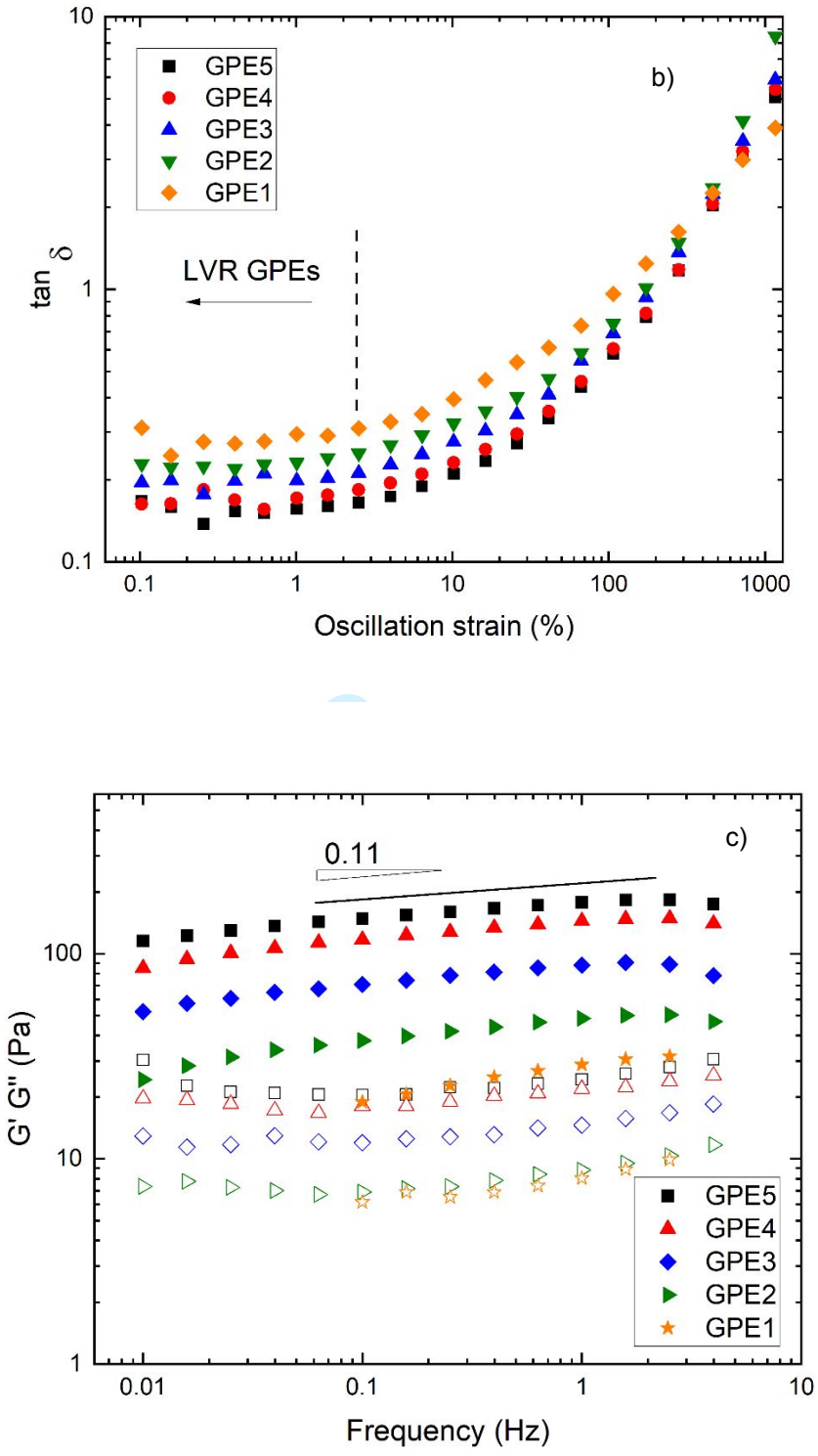

Figure 6. Oscillatory rheometry: Strain and frequency sweeps for GPEs. a) Log-log plot of *G′* (solid symbols), and *G″* (open symbols), as function of strain amplitude at 1 Hz. b) tan δ as function of strain amplitude at 1 Hz. c) Log-log plot of *G′* and *G″* as function of frequency at 0.1 % strain, located in LVR.

Determination of linear domain is observed in figure 6a. Storage *G′* and loss *G″* moduli are represented as function of oscillation strain amplitude, for all GPEs. At low strains, both moduli are independent of strain up to 4 % (except for GPE1, up to 2.5 %), indicating the linear viscoelastic region (LVR). In this region, *G′* is greater than *G″* for all the samples analyzed, demonstrating that the elastic portion of the material dominates in the linear regime. When a critical deformation is reached, moduli start to drop before reaching the crossover point. Beyond this critical strain deformation, the viscous modulus *G″* is greater than the elastic modulus *G′* as the sample is in its fluidized state.

Finally, As PAA concentration increases in GPEs, magnitude of storage and loss moduli increases. This result was expected as the addition of more gelling agent in the formulation results in a material with higher elasticity.

An equivalent representation of linear domain is observed in figure 6b, where tan δ (*G″/G′*) is represented as function of oscillation strain. As strain increases, it is seen that ratio between both moduli is constant up to a strain of 2.5 % for GPE1 and 4 % for the rest of GPEs. This result confirms the LVR as previously obtained directly from *G′*, *G″* as function of strain (figure 6a).

GPEs linear viscoelastic behavior is observed in figure 6c, where *G′* and *G″* are represented as function of frequency. Experiment was performed at a deformation of 0.1 %, located in LVR. From this test it is seen that in the range of frequency analyzed, *G′* is always greater than *G″*, revealing the desired gel behavior. Therefore, this result shows that even at highly alkaline environment in which pH > 14, it is possible to prepare gelled networks using PAA as gelling agent. In fact, there is no moduli crossover happening in the range of frequencies analyzed. This is also reflected in the slight dependence of GPEs to frequency. Elastic modulus behaves following weak power law with an average slope of 0.11, as observed in figure 6c, indicating slight dependence to frequency.

As PAA gel concentration decreases, both moduli value decreases, but gel-like behavior is still observed for all GPE samples at the lowest frequency tested. Furthermore, oscillations frequencies lower than 0.01 Hz become very irregular for GPE1 because of the low oscillatory torque, so results for this sample range between 0.1 and 4 Hz.

Gel behavior is interesting because incorporates mechanical resistance from the elastic solid behavior, being a good candidate to host zinc particles. In order to determine flow behavior, high deformation measurements were performed and they are depicted in the following section.

GPEs flow behavior

Steady state

Large deformation tests were performed not only to investigate flow behavior in the non-linear regime but also to evaluate the liquid-solid transition.

Shear stress as function of shear rate for the different GPEs is shown in figure 7. These results were obtained using decreasing shear steps as mention in section *GPEs flow curves*.

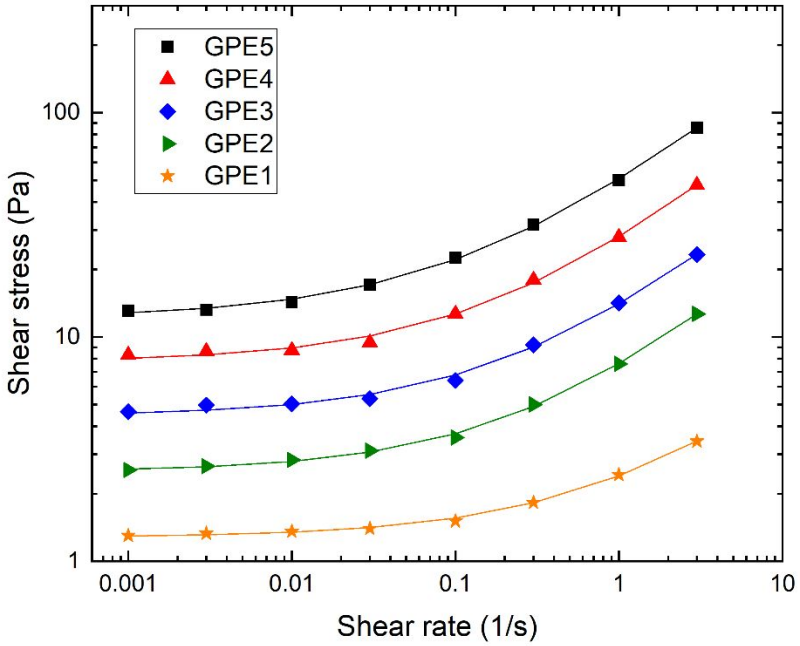

Figure 7. GPEs shear stress as function of shear rate. Closed symbols represent steady state measurement. Solid line represents data fitted to Herschel-Bulkley model (Equation 1).

It is seen that GPEs follow a yield stress fluid behavior. In fact, at low shear rates there is a tendency to reach a shear stress plateau indicating sample dynamic yield stress. Then, as shear rate increases, shear stress increases following a shear-thinning behavior. Shear stresses obtained at shear rates $\dot{\gamma} > 3\ s^{-1}$ were not considered because no steady state was found due to the presence of an elastic instability in the vane-in-cup (supplementary information S4). As expected, when PAA concentration increases (from GPE1 to GPE5), shear stress values increase, meaning that there is viscosity increase together with PAA concentration.

For each GPE considered in this study, experimental data was well fitted by a Herschel-Bulkley model (equation 1). Fitting can be observed in figure 7, represented by solid lines for each GPE. Herschel-Bulkley fitting parameters are summarized in table 2.

Sample	PAA [wt. %]	τ_y [Pa]	K [Pa s^n]	n [-]	R^2
GPE1	0.30	1.28	1.12	0.60	0.99
GPE2	0.45	2.51	5.09	0.63	
GPE3	0.60	4.44	9.62	0.62	
GPE4	0.75	7.75	20.27	0.61	
GPE5	0.90	12.15	38.58	0.59	

Table 2. GPEs yield stress extracted from Herschel-Bulkley fitting (equation 1).

It is observed from table 2 that yield stress τ_y increases with increasing PAA concentration, without significant changes in n flow indexes at different PAA concentrations, showing an identical shear-thinning behavior (n<1) in the range of PAA concentrations studied. Finally, consistency index K increases as PAA concentration increases.

To study the solid-liquid transition, creep experiments were exploited and analyzed to compare yield stress and viscosity behavior from flow curves.

Creeps

GPEs yielding

To determine sample static and dynamic yield stress, creep experiments were performed. Consecutive creeps (following protocol in figure 4a), for GPE5 can be seen in figure 8. This sample is chosen as an example as the same general behavior was found for the other GPEs.

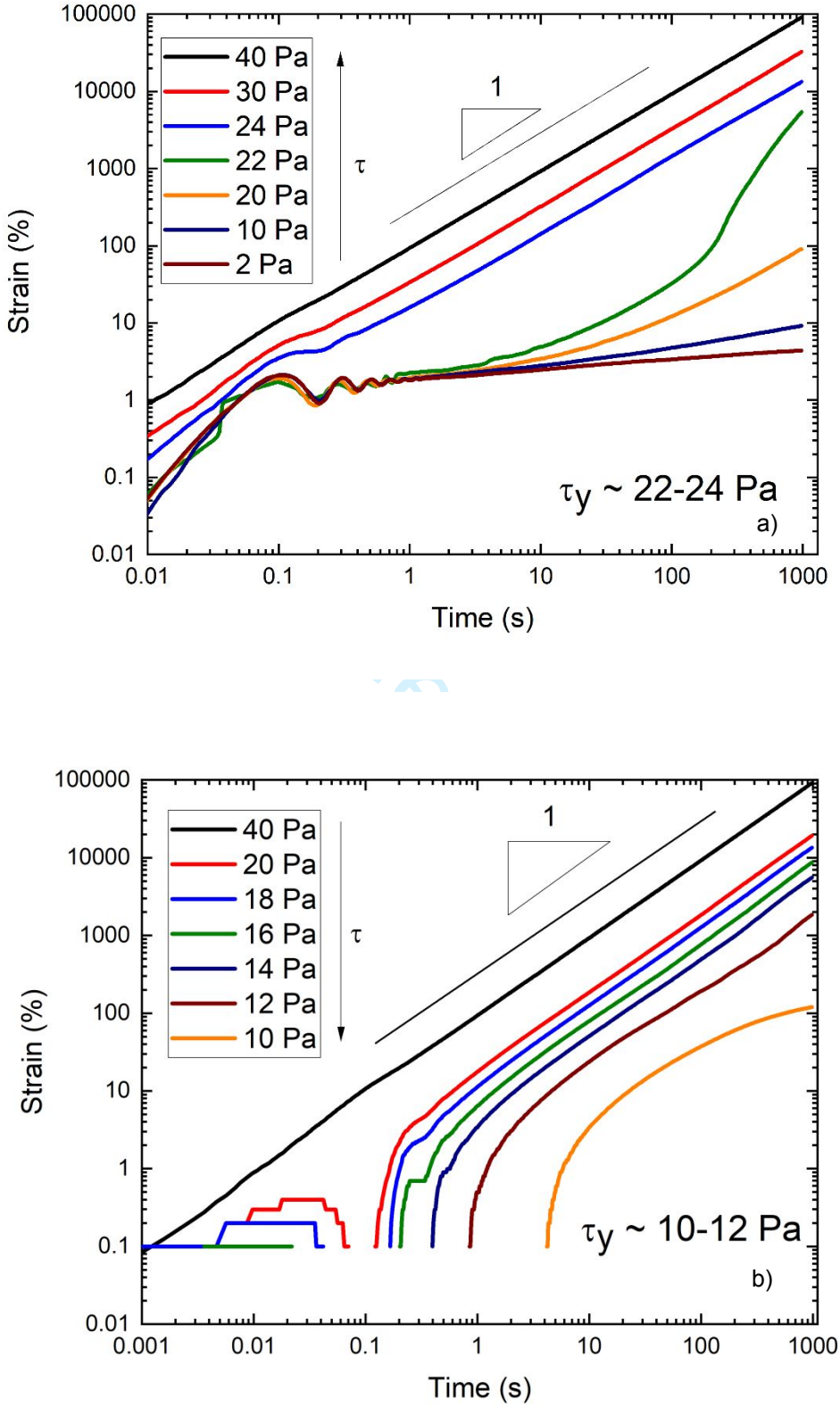

Figure 8. Successive creeps for GPE5. a) Increasing τ steps. b) Decreasing τ steps. $\Delta\tau$ = 2 Pa, Δt = 1000 s.

Figure 8a shows the evolution of strain as a function of time for increasing applied stresses, studying GPE5 solid-liquid transition. Note that the value of strain is set to zero at the start of each creep step in order to preserve accuracy and avoid rounding errors which become dominant for total strains larger than 10. For a better reading, only the most important steps are shown. From lower to higher stresses, strain oscillations appear at t < 1 s and are superposed one to each other. At t > 1 s strain increases as a weak power law of time, typical of solids in their creep regime. However, as shear stress is further increased to τ = 20 Pa, a different behavior is observed in which strain at t > 1 s increases significantly. Finally, when applying stresses equal and higher than 24 Pa, strain increases rapidly with a power law of 1, indicating that the sample is flowing. The transition between these two behaviors is observed and **static** yield stress of a value approximatively 22 - 24 Pa is observed considering this protocol and time-scale.

Figure 8b shows creep steps obtained by decreasing stresses. Note that oscillations with negative values cannot be represented in the log-log representation. From all the curves displayed in figure 8b, only creeps with τ equal to 12 and 10 Pa do not follow a power law of 1. Hence, the value of approximate 10 - 12 Pa denotes the **dynamic** yield stress.

From creep tests shown in figure 8, it is possible to observe inertio-elastic oscillations at t < 1 s. The analysis done with these oscillations in next section allows us to observe if sample viscoelastic properties change during a succession of decreasing creep steps.

Inertio-elastic oscillations

Inertio-elastic oscillations obtained from decreasing creeps steps are fitted to Jeffrey model (equation 6). A fitting for GPE5 is seen in figure 9. As a result, strain oscillations for this sample are well defined and can be analyzed with the model presented (Benmouffok-Benbelkacem et al. 2010).

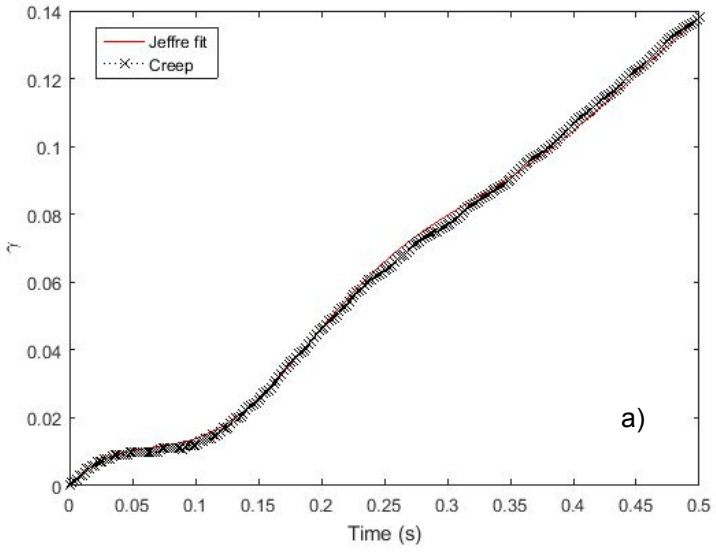

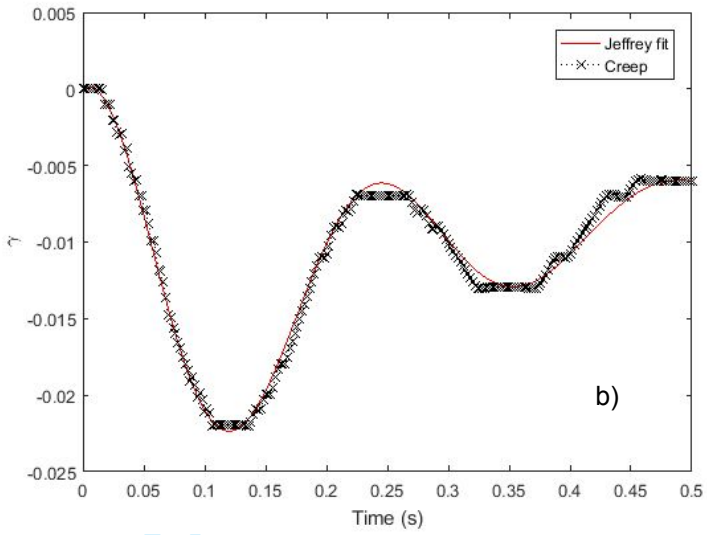

Figure 9. Fitting of strain as function of time for GPE5 obtained by decreasing shear stress steps. Fitting curve corresponds to the red solid line. a) Oscillations during GPE5 creep at 24 Pa. $\tau > \tau_y$. b) Oscillations during GPE5 creep at 12 Pa. $\tau \approx \tau_y$.

Figure 9 shows that Jeffrey model is able to fit data very well above and close to yield stress. Figure 9a shows the fitting for a creep performed at 24 Pa. Strain oscillates around a linear increase, showing that flow is developed indicating a viscoelastic fluid. This response was expected because 24 Pa is above GPE5 dynamic yield stress, as seen in figure 7 and 8b. Correspondingly, figure 9b shows the fitting for a creep performed at 12 Pa, very close to GPE5 yield stress. At this stress, it is possible to observe the elastic response in form of oscillations, belonging to the solid-elastic properties of GPE5.

From fitting strain experimental values to Jeffrey model (equation 6), elasticity *G*, elastic dissipation η_1 and viscosity η_2 are represented for GPE5. Steady state viscosity η_{ss} obtained from each creep is also represented. Results are shown in figure 10.

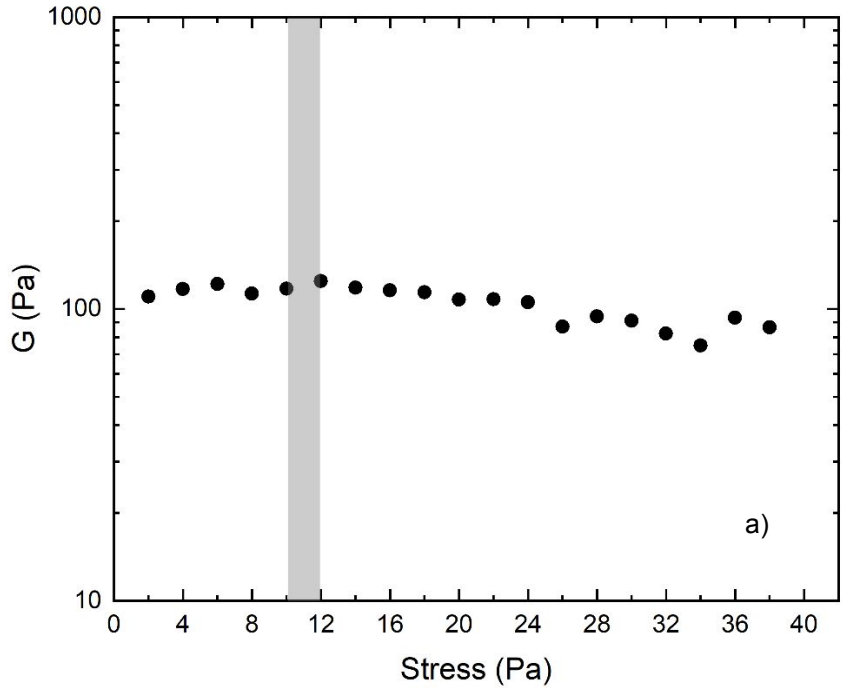
1000
100
10
G (Pa)
a)
0
4
8
12
16
20
24
28
32
36
40
Stress (Pa)

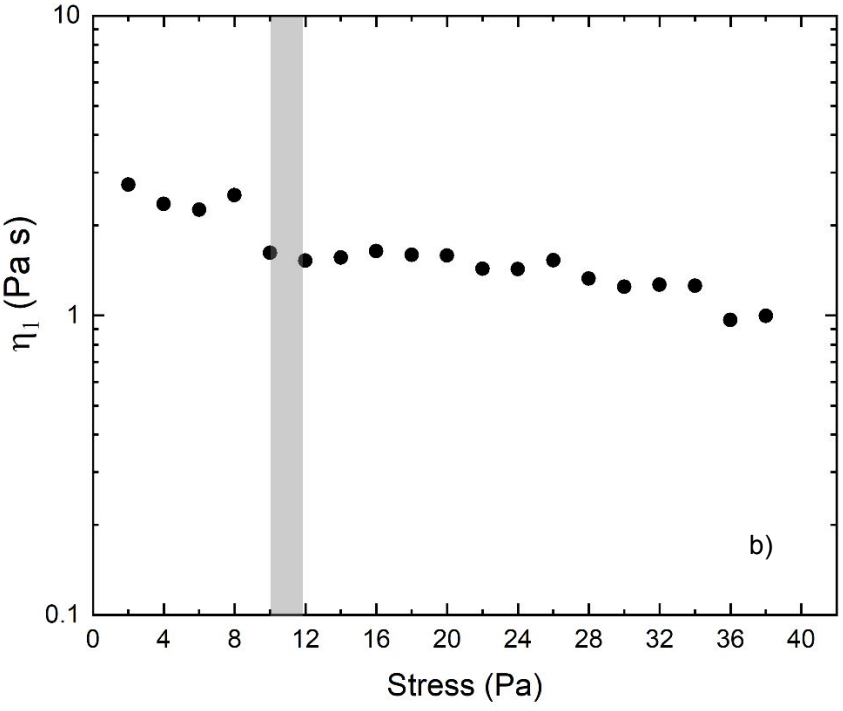
10
1
0.1
η1 (Pa s)
b)
0
4
8
12
16
20
24
28
32
36
40
Stress (Pa)

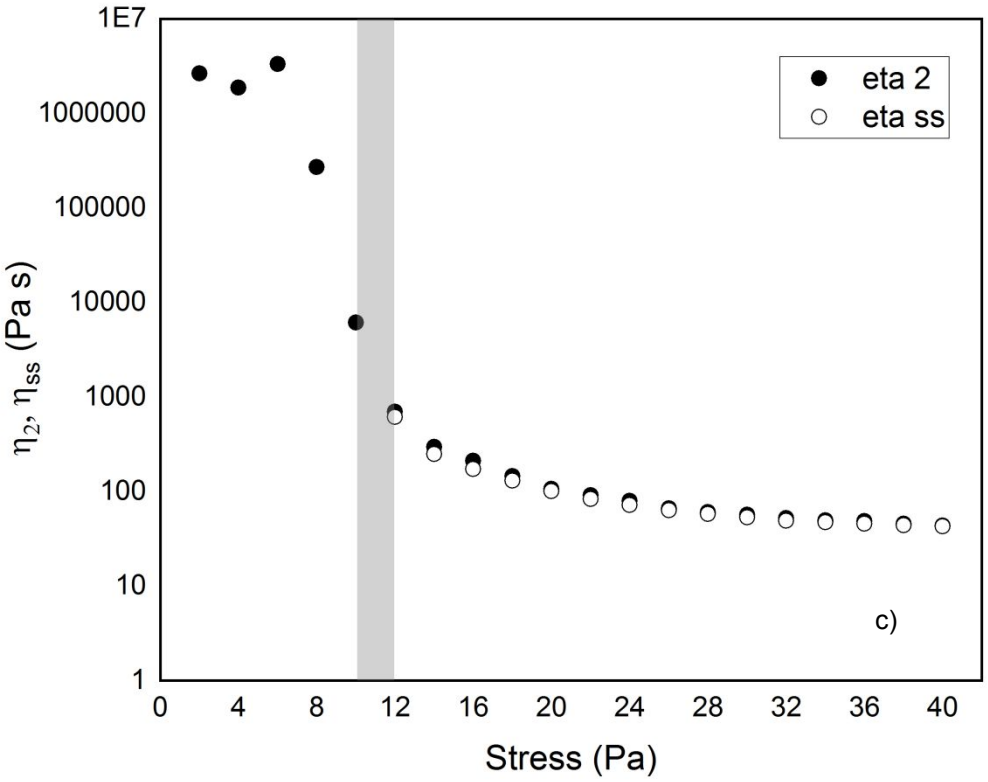

Figure 10. Fitting parameters for GPE5 obtained from decreasing successive creeps with a step duration of 1000 s. Yield stress τ_y obtained from Herschel-Bulkley fitting is highlighted in gray. a) Elasticity *G* as function of shear stress. b) η_1 as function of shear stress. c) η_{ss} (open symbols) and η_2 (solid symbols) as function of shear stress.

In figure 10a, elasticity *G* is analyzed. *G* remains constant at $\tau < \tau_y$ (yield stress from Herschel-Bulkley fitting is highlighted in grey). At $\tau > \tau_y$, *G* remains stable up to a stress value of 24 Pa. At stresses 24 < $\tau \leq 40$, *G* values are slightly lower compared to the value obtained below yield stress.

Elastic dissipation η_1 is observed in figure 10b. At $\tau < \tau_y$, η_1 is constant and shows higher values compared to the behavior at $\tau > \tau_y$, where η_1 decreases progressively as stress increases, down to 38 % of the value obtained below yield stress.

Finally, in figure 10c it is possible to observe the behavior of viscosity η_2 and η_{ss} as function of shear stress. In here, η_2 obtained from Jeffrey model (equation 6) at the beginning of each creep step (t < 1 s) is compared with the viscosity η_{ss} obtained at the end of each creep step. This comparison allows to determine if material presents significant retarded thixotropy or viscoelasticity on a time scale of about Δt = 1000 s (see (Benmouffok-Benbelkacem et al. 2010)). From this result, it is possible to observe that both viscosities converge at stresses $\tau > \tau_y$ when down ramping shear stress steps. This result means that in the sample fluidized-state, no time-dependent behavior is observed, like in neutral Carbopol®

gels (Caton and Baravian 2008; Benmouffok-Benbelkacem et al. 2010). Contrarily, when $\tau < \tau_y$, viscosity η_2 forms a plateau, whereas η_{ss}, given by the rheometer, is not representative of the sample as GPE is not flowing (strain tends to decrease indefinitely at these stresses), and therefore no viscosity can be associated to it.

Discussion

GPEs rheological characterization at small and large deformations are important as gels are prepared to host dense zinc particles in a RFB. Indeed, gels have to behave as yield stress fluids to ensure a good performance of the slurry during charge and discharge of the battery. For slurry RFBs, it is necessary that an interconnected particle network is present to enhance the conductivity of the slurry. As mentioned previously, zinc particles have a density of 7.13 g/cm^3 and are to be suspended in harsh alkaline conditions (pH > 14). Therefore, it is mandatory to ensure yield stress properties for zinc slurry - air RFBs with the formulation proposed in this study.

Gel behavior was throughout investigated as it is crucial to avoid sedimentation of zinc particles. Small deformation tests allowed characterization representative of sample at rest, important for RFB application when the battery is not operating (zero flow through the battery reactor). Frequency sweeps performed at a deformation located in the linear regime (0.1 %), demonstrated that all GPEs behave as a gel material: *G′* is greater than *G″* at all frequencies tested and there is no moduli crossover (figure 6c), as the dependence of the moduli towards the frequency is weak.

Furthermore, when applying decreasing steps, dynamic yield stress was determined for each sample. It was found that all samples behaved as yield stress fluids, property that is crucial to maintain zinc particles in suspension. It was found that values obtained by creeps correspond to the ones determined with Herschel-Bulkley fitting (table 2), as depicted in figure 11.

From these results it is observed that there is a good agreement in characterizing the liquid-solid transition with both shearing methods. As PAA concentration increases, yield stress values gradually increases. It is seen that in the range of concentrations studied, yield stress values follow a power law:

$$\tau_y = 13.6(PAA)^{1.83} \qquad (7)$$

Where PAA is the polymer concentration in wt. %.

These results suggest that regardless of the method used to determine GPEs yield stress, fluid behavior will be the same if sample is characterized by imposing decreasing shearing steps, as stated by Ovarlez et al. (Ovarlez et al. 2013) and N'gouamba et al. (N'gouamba et al. 2020). More precisely, Ovarlez et al. found that when increasing shear rates, unsheared regions corresponding to material solid behavior are present across the sample. These heterogeneous stress fields can appear, as destructuration and restructuration physical phenomenon are in competition when sample undergoes a transition from a

solid to fluid-like behavior. Further comparison of yield stress obtained from creeps and Herschel-Bulkley fitting can be observed in supplementary information S5.

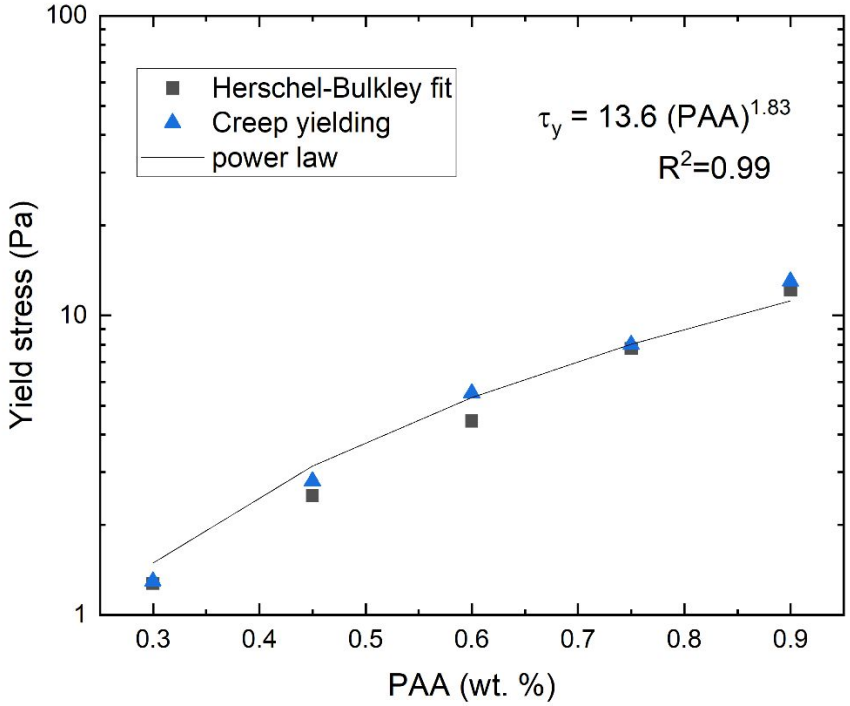

Figure 11. Yield stress τ_y as function of PAA concentration obtained by strain-controlled and stress-controlled experiments.

Correspondingly, GPEs behavior in the fluidized state is very important for the operation of the battery. Viscosity decrease is critical in RFB systems, as lower viscosities will require less energy for pumping (Iyer et al. 2017), improving global energetic efficiency. Moreover, lower viscosities reduce ohmic and mass-transfer resistances, leading to more efficient and feasible processes (Barton et al. 2018). By performing large deformation tests, either by imposing shear rate (figure 7) or creeps (figure 10c), it was found that in the fluidized state, GPEs behave as shear-thinning fluids. This result is essential as it allows to consider the GPEs presented in this study as good candidates for actual slurry formulation, given that their viscosity will decrease when gels subjected to pumping through the battery during operation.

Conclusion

This study is a rheological approach on the study of PAA-based gels at alkaline conditions. With the formulation presented in here, using PAA together with attapulgite as gelling agents, it was possible to prepare gels possessing a yield stress and shear-thinning behaviour in highly alkaline conditions (10 M KOH). Elasto-visco-plastic properties were found for all GPEs through small and large deformation rheological tests using a Couette analogy approach and a tailored characterisation protocol.

This study broadens the use of traditional gelling agents to a harsh alkaline environment in which gel behavior is still present. This study can bring more attention to the formulation of GPEs to prepares slurries in non-neutral environments for RFB application.

Acknowledgements

This project has received funding from the European Union's Horizon 2020 research and innovation programme under the Marie Skłodowska-Curie Grant Agreement number 765289.

Conflicts of interest

The authors declare no conflict of interest.

Glossary
List of variables

Symbol	Description	Units
τ	Shear stress	Pa
γ	Strain	-
$\dot{\gamma}$	Shear rate	s^{-1}
τ_y	Yield stress	Pa
K	Consistency index	Pa s^n
n	Flow index	-
η_{ss}	Steady state viscosity	Pa s
η_1	Elastic dissipation	Pa s
η_2	Viscosity (Jeffrey model)	Pa s
G	Elasticity (Jeffrey model)	Pa
G'	Elastic modulus	Pa
G''	Viscous modulus	Pa
$K_{\dot{\gamma}}$	Shear rate geometrical constant	Rad^{-1}
K_{τ}	Shear stress geometrical constant	Pa $N^{-1}m^{-1}$
$\dot{\theta}$	Rotational speed	Rad s^{-1}
Γ	Torque	N m
R_e	Cup radius	m
R_i	Analogous inner cylinder radius	m
h	Height of the vane geometry	m
r^*	Optimal radial position	m

References

Aït-kadi A, Marchal P, Choplin L, Bousmina M (2002) Quantitative Analysis of Mixer-Type Rheometers. The Canadian Journal of Chemical Engineering 80:1166–1174

Auffret Y, Roux DCD, el Kissi N, et al (2009) Aging and yielding in a sheared AOT/iso-octane/water lyotropic lamellar phase. European Physical Journal E 29:51–60. https://doi.org/10.1140/epje/i2009-10450-6

Banik SJ, Akolkar R (2015) Suppressing Dendritic Growth during Alkaline Zinc Electrodeposition using Polyethylenimine Additive. Electrochimica Acta 179:475–481. https://doi.org/10.1016/j.electacta.2014.12.100

Baravian C, Lalante A, Parker A (2002) Vane rheometry with a large, finite gap. Applied Rheology 12:81–87. https://doi.org/10.1017/S0022029998003057

Baravian C, Quemada D (1998) Using instrumental inertia in controlled stress rheometry. Rheologica Acta 37:223–233. https://doi.org/10.1007/s003970050110

Barnes HA, Nguyen QD (2001) Rotating vane rheometry-a review. Journal of Non-Newtonian Fluid Mechanics 98:1–14

Barton JL, Milshtein JD, Hinricher JJ, Brushett FR (2018) Quantifying the impact of viscosity on mass-transfer coefficients in redox flow batteries. Journal of Power Sources 399:133–143. https://doi.org/10.1016/j.jpowsour.2018.07.046

Benmouffok-Benbelkacem G, Caton F, Baravian C, Skali-Lami S (2010) Non-linear viscoelasticity and temporal behavior of typical yield stress fluids: Carbopol, Xanthan and Ketchup. Rheologica Acta 49:305–314. https://doi.org/10.1007/s00397-010-0430-4

Bockelmann M, Kunz U, Turek T (2016) Electrically rechargeable zinc-oxygen flow battery with high power density. Electrochemistry Communications 69:24–27. https://doi.org/10.1016/j.elecom.2016.05.013

Caton F, Baravian C (2008) Plastic behavior of some yield stress fluids: From creep to long-time yield. Rheologica Acta 47:601–607. https://doi.org/10.1007/s00397-008-0267-2

Charman WN, Christy DP, Geunin EP, Monkhouse DC (1991) Interaction between calcium, a model divalent cation, and a range of poly (acrylic acid) resins as a function of solution ph. Drug Development and Industrial Pharmacy 17:271–280. https://doi.org/10.3109/03639049109043824

Cheng DCH (1986) Yield stress: A time-dependent property and how to measure it. Rheologica Acta 25:542–554. https://doi.org/10.1007/BF01774406

Choi NH, del Olmo D, Fischer P, et al (2020a) Development of flow fields for zinc slurry air flow batteries. Batteries 6:15. https://doi.org/10.3390/batteries6010015

Choi NH, del Olmo D, Milian D, et al (2020b) Use of carbon additives towards rechargeable Zinc Slurry Air Flow Batteries. Energies 13:4482. https://doi.org/10.3390/en13174482

Ciez RE, Whitacre JF (2016) The cost of lithium is unlikely to upend the price of Li-ion storage systems. Journal of Power Sources 320:310–313. https://doi.org/10.1016/j.jpowsour.2016.04.073

Dinkgreve M, Paredes J, Denn MM, Bonn D (2016) On different ways of measuring “the” yield stress. Journal of Non-Newtonian Fluid Mechanics 238:233–241. https://doi.org/10.1016/j.jnnfm.2016.11.001

Duduta M, Ho B, Wood VC, et al (2011) Semi-solid lithium rechargeable flow battery. Advanced Energy Materials 1:511–516. https://doi.org/10.1002/aenm.201100152

Eitelberg G (1984) Corrigendum to Weissenberg effect and its dependence upon the experimental geometry. Rheologica Acta 23:327

Frigaard I (2019) Simple yield stress fluids. Current Opinion in Colloid and Interface Science 43:80–93

Garole DJ, Hossain R, Garole VJ, et al (2020) Recycle, Recover and Repurpose Strategy of Spent Li-ion Batteries and Catalysts: Current Status and Future Opportunities. ChemSusChem 13:3079–3100. https://doi.org/10.1002/cssc.201903213

Gruber PW, Medina PA, Keoleian GA, et al (2011) Global lithium availability: A constraint for electric vehicles? Journal of Industrial Ecology 15:760–775. https://doi.org/10.1111/j.1530-9290.2011.00359.x

Gu P, Zheng M, Zhao Q, et al (2017) Rechargeable zinc-air batteries: A promising way to green energy. Journal of Materials Chemistry A 5:7651–7666

Gutowski IA, Lee D, de Bruyn JR, Frisken BJ (2012) Scaling and mesostructure of Carbopol dispersions. Rheologica Acta 51:441–450. https://doi.org/10.1007/s00397-011-0614-6

Han X, Li X, White J, et al (2018) Metal–Air Batteries: From Static to Flow System. Advanced Energy Materials 8:1–28. https://doi.org/10.1002/aenm.201801396

Hermoso J, Jofore BD, Martínez-Boza FJ, Gallegos C (2012) High pressure mixing rheology of drilling fluids. Industrial and Engineering Chemistry Research 51:14399–14407. https://doi.org/10.1021/ie301835y

Iyer VA, Schuh JK, Montoto EC, et al (2017) Assessing the impact of electrolyte conductivity and viscosity on the reactor cost and pressure drop of redox-active polymer flow batteries. Journal of Power Sources 361:334–344. https://doi.org/10.1016/j.jpowsour.2017.06.052

Kim H, Jeong G, Kim YU, et al (2013) Metallic anodes for next generation secondary batteries. Chemical Society Reviews 42:9011–9034

Kong L, Li C, Jiang J, Pecht MG (2018) Li-ion battery fire hazards and safety strategies. Energies 11:1–11. https://doi.org/10.3390/en11092191

Li M, Lu J, Chen Z, Amine K (2018) 30 Years of Lithium-Ion Batteries. Advanced Materials 30

Liu Z, Pulletikurthi G, Lahiri A, et al (2016) Suppressing the dendritic growth of zinc in an ionic liquid containing cationic and anionic zinc complexes for battery applications. Dalton Transactions 45:8089–8098. https://doi.org/10.1039/c6dt00969g

Lochhead RY, Davidson JA, Thomas GM (1989) Poly(acrylic acid) thickeners. The importance of gel microrheology and evaluation of hydrophobically modified derivatives as emulsifiers. AdvChemSer 223:113–147

Mainar AR, Colmenares LC, Grande HJ, Blázquez JA (2018a) Enhancing the cycle life of a Zinc–air battery by means of electrolyte additives and zinc surface protection. Batteries 4:. https://doi.org/10.3390/batteries4030046

Mainar AR, Iruin E, Colmenares LC, et al (2018b) An overview of progress in electrolytes for secondary zinc-air batteries and other storage systems based on zinc. Journal of Energy Storage 15:304–328. https://doi.org/10.1016/j.est.2017.12.004

Mainar AR, Iruin E, Colmenares LC, et al (2018c) Systematic cycle life assessment of a secondary zinc–air battery as a function of the alkaline electrolyte composition. Energy Science and Engineering 6:174–186. https://doi.org/10.1002/ese3.191

Mainar AR, Olatz L, Bengoechea M, et al (2016) Alkaline aqueous electrolytes for secondary zinc-air batteries: an overview. International Journal of Energy Research 40:1032–1049. https://doi.org/10.1002/er

Møller PCF, Mewis J, Bonn D (2006) Yield stress and thixotropy: On the difficulty of measuring yield stresses in practice. Soft Matter 2:274–283. https://doi.org/10.1039/b517840a

N'gouamba E, Goyon J, Tocquer L, et al (2020) Yielding, thixotropy, and strain stiffening of aqueous carbon black suspensions. Journal of Rheology 64:955–968. https://doi.org/10.1122/8.0000028

Ovarlez G, Cohen-Addad S, Krishan K, et al (2013) On the existence of a simple yield stress fluid behavior. Journal of Non-Newtonian Fluid Mechanics 193:68–79. https://doi.org/10.1016/j.jnnfm.2012.06.009

Ovarlez G, Mahaut F, Bertrand F, Chateau X (2011) Flows and heterogeneities with a vane tool: Magnetic resonance imaging measurements. Journal of Rheology 55:197–223. https://doi.org/10.1122/1.3526349

Ovarlez G, Mahaut F, Deboeuf S, et al (2015) Flows of suspensions of particles in yield stress fluids. Journal of Rheology 59:1449–1486. https://doi.org/10.1122/1.4934363

Owens CE, Hart AJ, McKinley GH (2020) Improved rheometry of yield stress fluids using bespoke fractal 3D printed vanes. Journal of Rheology 64:643–662. https://doi.org/10.1122/1.5132340

Piau JM (2007) Carbopol gels: Elastoviscoplastic and slippery glasses made of individual swollen sponges. Meso- and macroscopic properties, constitutive equations and scaling laws. Journal of Non-Newtonian Fluid Mechanics 144:1–29. https://doi.org/10.1016/j.jnnfm.2007.02.011

Puig J, Hanotin C, Neyret M, Marchal P (2016) High temperature rheological study of borosilicate glasses containing platinum group metal particles by means of a mixer-type rheometer. Journal of Nuclear Materials 469:112–119. https://doi.org/10.1016/j.jnucmat.2015.11.053

Rugolo J, Aziz MJ (2012) Electricity storage for intermittent renewable sources. Energy and Environmental Science 5:7151–7160. https://doi.org/10.1039/c2ee02542f

Sonneveld PJAN (1991) The zinc suspension electrode

Tran TNT, Chung HJ, Ivey DG (2019) A study of alkaline gel polymer electrolytes for rechargeable zinc–air batteries. Electrochimica Acta 327:135021. https://doi.org/10.1016/j.electacta.2019.135021

Vikström H, Davidsson S, Höök M (2013) Lithium availability and future production outlooks. Applied Energy 110:252–266. https://doi.org/10.1016/j.apenergy.2013.04.005

Weissenberg K (1947) A continuum theory of rheological phenomena. Nature 159:310–311. https://doi.org/https://doi.org/10.1038/159310a0

Yang C, Zhang Z, Tian Z, et al (2016) Effects of Carboxymethyl Cellulose on the Electrochemical Characteristics and Dendrite Growth of Zinc in Alkaline Solution. Journal of The Electrochemical Society 163:A1836–A1840. https://doi.org/10.1149/2.0101609jes

Yang H, Cao Y, Ai X, Xiao L (2004) Improved discharge capacity and suppressed surface passivation of zinc anode in dilute alkaline solution using surfactant additives. Journal of Power Sources 128:97–101. https://doi.org/10.1016/j.jpowsour.2003.09.050

Yao NY, Larsen RJ, Weitz DA (2008) Probing nonlinear rheology with inertio-elastic oscillations. Journal of Rheology 52:1013–1025. https://doi.org/10.1122/1.2933171

Supplementary information

Gel polymer electrolytes rheological behavior: yield stress and viscoelasticity

Diego Milián[a], Denis C.D. Roux[a], François Caton[a], Nadia El Kissi[a]

[a]*Univ. Grenoble Alpes, CNRS, Grenoble INP, LRP, 38000 Grenoble, France*

S1 Analogous cylinder radius and optimal radial position

To determine the analogous radius of the inner cylinder R_i, an experiment in which torque as function of rotational velocity is determined using a fluid of known consistency and flow index (Newtonian fluid ISO 17025, 6166 mPa s, 20 ºC, Paragon Scientific Ltd). Then, R_i is determined as follows:

$$R_i = \frac{R_e}{\left[1 + \frac{2\dot{\theta}}{n}\left(\frac{2\pi K h R_e^2}{\Gamma}\right)^{\frac{1}{n}}\right]^{\frac{n}{2}}} \qquad (1)$$

By substituting torque Γ and rotational velocity $\dot{\theta}$ obtained by shearing a fluid with well-known rheological properties (*n, K*), using the vane-in-cup geometry (vane height *h* and cup radius R_e), an internal radius R_i = 13 mm for an analogous cylinder is obtained.

The optimal radial position *r**, in which $K_{\dot{\gamma}}$ is independent of *n*, is calculated as follows in the range of flow indexes [*n*, *n'*]:

$$r^* = \left[\frac{n'\left(\frac{R_e}{R_i}\right)^{\frac{2}{n'}} - 1}{n\left(\frac{R_e}{R_i}\right)^{\frac{2}{n}} - 1} R_e^{\left(\frac{2}{n} - \frac{2}{n'}\right)}\right]^{\frac{1}{\left(\frac{2}{n} - \frac{2}{n'}\right)}} \qquad (2)$$

Where *n* and *n'* are the extreme flow indexes representing the range of shear thinning fluids to be studied. To do the calibration, values of *n* = 1 and *n'* = 0.2 were chosen and a value of *r** = 15 mm was obtained. In this position *r**, $K_{\dot{\gamma}}$ and K_τ are calculated so both geometrical factors are independent of sample flow index, in the specified range.

Geometrical factors were validated by comparing shear stress as function of shear rate obtained with two different geometries for a Carbopol® gel (PAA) 0.10 wt. %, as depicted in figure S1. It is observed that a good agreement is found in the characterization of a yield stress fluid such as a Carbopol gel by using either cone and plate or vane-in-cup geometry.

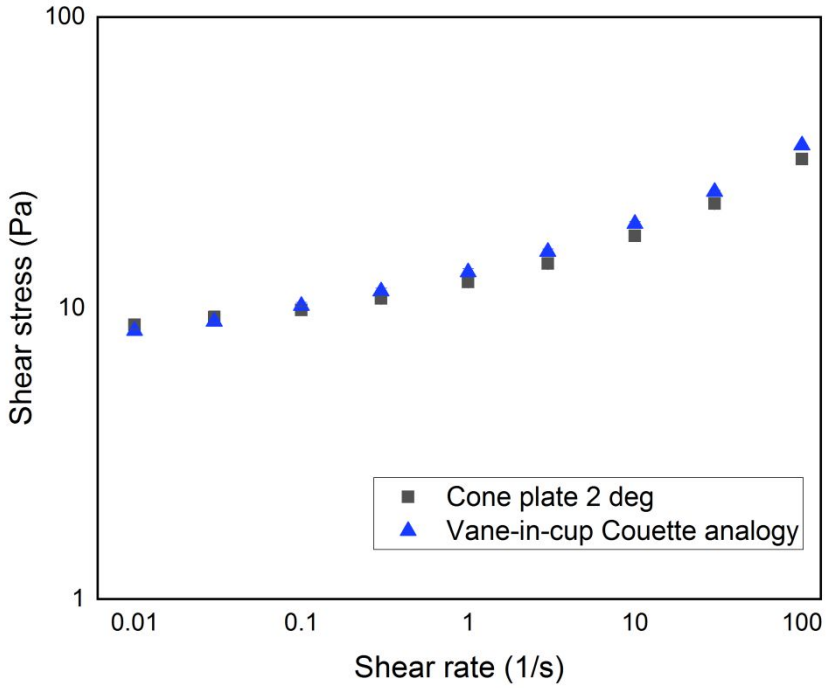

Figure S1. Shear stress as function of shear rate for PAA 0.10 wt. % using a vane-in-cup calibrated with Cup Analogy approach, and a cone and plane geometry.

S2 Weissenberg effect / Steady state Δt

Values represented in figure S2 at shear rates > 3 s^{-1} are the shear stress values obtained at the end of each shearing step, representing an apparent shear stress. Insets represent the appearance of the free surface area when shearing in a stable zone (white background) or unstable zone (red background). Measurements obtained within unstable zone belong to a transient state where no constitutive equation supports this phenomenon.

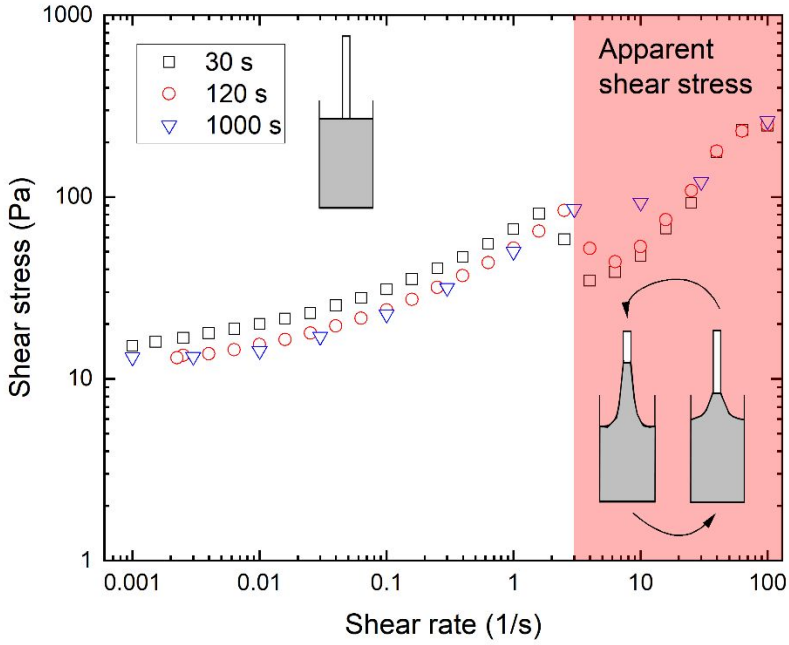

Figure S2. Shear stress as function of shear rate for GPE5 obtained by down ramping shear rate at different acquisition times: 30, 120 and 1000 s per point. Inset figure indicate sample free surface area while being sheared.

To determine the minimum shearing time to obtain steady state measurements, steps of variable durations were performed while decreasing shear rate. Shear durations Δt = 30, 120 and 1000 s were investigated and shown in figure S2. It is observed that by shearing just 30 s per point, steady state is not obtained as stress would have continued to decrease over time. On the other hand, it is seen that 120 s is almost enough to reach steady state, when it is compared to 1000 s per step.

S3 Sample appearance under shearing

Figure S3 shows stress response when shear rate is consecutively increased from 0.001 to 100 s^{-1} and then decreased to 0.001 s^{-1} (Δt = 120 s). Insets are pictures of sample appearance taken through the transparent cup. When performing the increasing shear rate steps, it is observed that sample appearance at 0.01 s^{-1} is plain and continuous, just like after GPE preparation. When shear rate increases to 1 s^{-1}, small defects start to be seen randomly. Finally, at shear rates > 3 s^{-1}, aggregates can be seen across the whole sample. Once small aggregates form, sample do not go back to its initial smooth appearance. After performing decreasing shear rate steps, sample appearance remains like the one obtained at 100 s^{-1}.

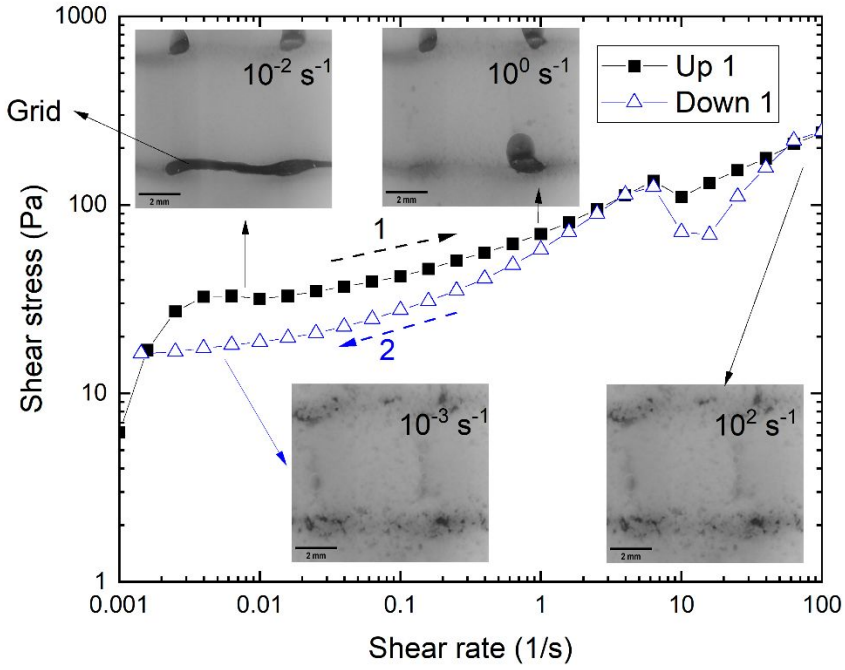

Figure S3. GPE5 appearance at different shear rates. Pictures were obtained through the transparent cup with a USB camera.

S4 Transient GPE behavior (Weissenberg effect)

Shear stress signal at different shear rates were recorded following the protocol in figure S4a. Shear stress response is obtained and shown in figure S4b for GPE5.

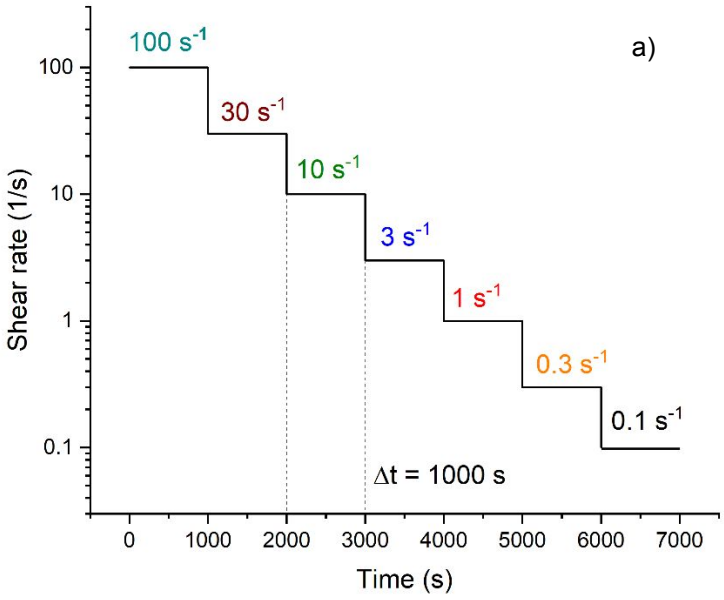

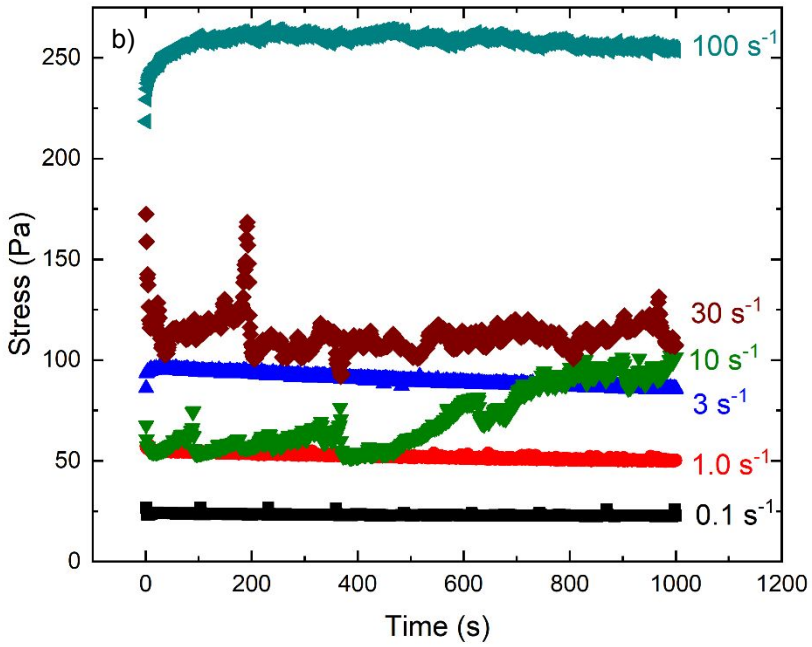

Figure S4. a) Steady state determination protocol. Sample undergoes consecutively decreasing shear rate steps from 100 to 0.001 s-1. Each step had a duration of 1000 s. b) Shear stress signal at different shear rates for GPE5.

Initially at 100 s^{-1} shear stress signal is somewhat stable, but small stress fluctuations are perceived as observed in figure S4b. When decreasing shear rate to 30 and 10 s^{-1}, shear stress signal starts to fluctuate significantly, and steady state behavior is not found. Shear rates higher than 3 s^{-1} produce a phenomenon in which shear stress undershoots as the volume of sheared sample is continuously changing: material tries to climb the shearing geometry, similarly to rod climbing (Weissenberg effect). This can be observed in the video attached in supplementary information. As the sheared volume changes, rheometer struggles to keep up with the imposed shear rate. At shear rate values of 3 s^{-1} and lower, shear stress signal remains stable over time denoting steady state. Because of this, the range of shear rates explored in this study corresponds to ≤ 3 s^{-1}, where no perturbations are observed and steady state is reached for all samples.

S5 Yield stress τ_y method obtention comparison

Steady state viscosity obtained from creeps as function of shear stress is depicted in figure S5.

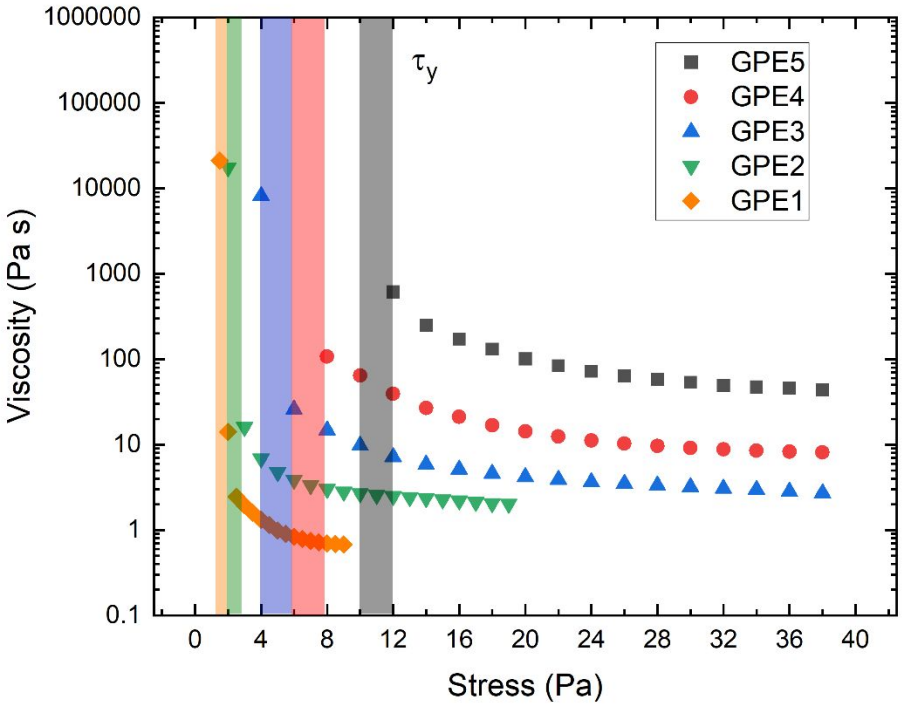

Figure S5. GPEs viscosity as function of shear stress. Values of τ_y from Herschel-Bulkley fitting are represented with colored bars for each GPE.

In figure S5, viscosity as function of shear stress is plotted for each GPE. Moreover, τ_y obtained from Herschel-Bulkley is represented as a vertical bar for each GPE. It can be seen that viscosity decreases significantly when stresses are higher than the τ_y from the Herschel-Bulkley model. Therefore, there is a good agreement in characterizing the liquid-solid transition with both methods. Shear thinning behavior is observed as shear stress values increases. Finally, as PAA concentration increases, viscosity is found to be higher, as expected.